Optimization of thermal barrier coating performance and durability over a drive cycle

Georgios Koutsakis and Jaal B Ghandhi

Abstract

A methodology to thermo-mechanically optimize a piston thermal barrier coating over a full drive cycle was established. The optimization objective was to minimize the heat transfer to the engine wall while maintaining structural integrity of the coating. Over 800 candidate materials were investigated and the optimization required more than one million non-road transient drive cycle calculations; real materials were investigated to ensure a realizable result and the existence of thermal and mechanical properties. High computational efficiency was achieved using a recently developed analytical heat transfer technique for multilayer engine walls. An uncoupled approach was utilized for the optimization, wherein the gas temperature and heat transfer coefficient profiles from a fully coupled and calibrated baseline model over the 20-min drive cycle were employed. The coating/piston interface temperature was constrained to be below the maximum piston service temperature limit. The durability was assessed using a recently developed analytical coating delamination framework for engine in-cylinder coatings based on the energy release rate when a crack forms. Results are presented for a mechanically unconstrained optimization and for cases constrained to three fixed levels of drive-cycle maximum energy release rate, and also constrained by the individual material's toughness. The best-performing coating materials identified were verified using the fully coupled system-level model, which compared well to the uncoupled predictions. A study on the effect of adding a sealing layer to some high-performing, but porous, coatings showed a reduction in fuel consumption benefit and an increased exhaust temperature over the cycle, but the system still outperformed the uncoated case. The results of the study elucidate the importance of including engine performance and mechanical failure considerations in thermal barrier coating design.

Introduction

The issues associated with greenhouse gases and climate change will likely incentivize new mobile powertrain solutions in the future. Because it is currently the most cost-effective powertrain option available, however, improvements in the combustion, aftertreatment strategies, and engine thermal management of internal combustion (IC) engines continue to be necessary. With proper design, an IC engine with optimized efficiency will be a difficult target to overtake. One potential pathway to increasing thermal efficiency is to reduce heat loss to the cylinder walls.[1]

Heat transfers from the high temperature gas to the combustion chamber surfaces because of their temperature difference. There is a significant interest in the application of thin, low-thermal-conductivity, k, low-volumetric-heat-capacity, ρc, thermal barrier coatings to combustion chamber surfaces. These coatings can better follow the rapid gas temperature swings and, thus, reduce the gas-wall surface temperature differential that drives heat transfer.

There have been a large number of experimental and numerical studies of thermal barrier coatings as

Engine Research Center, University of Wisconsin–Madison, Madison, WI, USA

Corresponding author:
Georgios Koutsakis, Engine Research Center, University of Wisconsin–Madison, 1500 Engineering Dr., B104, Madison, WI 53706, USA.
Email: koutsakis@wisc.edu

illustrated in a recent state-of-the-art literature review.[2] That review focused on the engine performance and emissions trade-offs associated with different coating characteristics, for example, thickness, porosity, and surface roughness. In addition, it also discussed how the gas-wall interface characteristics (velocity gradient, flame distribution, near-wall air-fuel mixture composition, and radiative heat transfer) affected the earlier engine performance studies. However, the existence of parametric or optimization investigations in the literature is limited. Existing studies have been performed: (i) for a steady state operation; (ii) with only a few coatings; and (iii) optimized only based on the engine thermal performance neglecting coating structural integrity.[3–12] A more comprehensive approach to material and thickness optimization of the thermal barrier coatings will be required to achieve targeted brake thermal efficiencies beyond 55%.[13–15]

Initial coating formulations showed mixed engine performance. Several authors reported a reduction in fuel consumption by using coated in-cylinder components,[16–19] but others reported comparable or worse fuel consumption.[19–23] More recent formulations have shown positive thermal efficiency results across the few steady state conditions tested, ranging from 0.5% to 1% gain.[4,6,11,24] A 5% fuel consumption benefit[5,25] was reported (based on experiments) after 1 min of cold start operation.

Researchers have studied the effects of soot deposits, surface roughness, and heat transfer coefficient on coated combustion chambers. Coated walls have shown reduced combustion chamber soot deposits on the piston periphery,[26] while homogeneous charge compression ignition (HCCI) operational range has been shifted to lower loads.[27] Increased surface roughness provides more effective area and can increase near-wall turbulence. Additionally, the air-fuel mixing process can be affected, which in turn, affects chemistry.[28] Minor efficiency improvements[9,29,30] have been shown for polished[31] thermal barrier coatings at high loads compared to the as-sprayed condition. The heat transfer coefficient has been suggested by some authors to increase[32–35] with the addition of a thermal barrier coating in comparison to an all-metal baseline engine. However, other studies indicated that the heat transfer coefficient remains unchanged.[16,23,36,37]

Combustion regimes such as conventional diesel combustion (CDC) and low-temperature-combustion (LTC) may have substantial spatial variations of heat flux over the cycle. An experimental investigation by Hendricks et al.[38] showed that CDC heat flux has higher non-uniformity relative to dual-fuel reactivity-controlled compression ignition (RCCI),[39,40] since the latter combustion occurs at a more uniform equivalence ratio and lower peak local combustion temperatures. Optical measurements from Kokjohn et al. demonstrated that RCCI heat-release rate spatial variations fall between CDC and that of a fully premixed combustion strategy, for example, homogeneous charge compression ignition (HCCI).

A calibrated, system-level model was used to assess engine performance over a full drive cycle for various multilayer coatings. The model was coupled with an analytical heat conduction solver for multi-layer walls,[41–43] which solved only for the instantaneous wall surface temperature. Unlike finite difference approaches that have numerical stability concerns and must evaluate the entire wall temperature distribution at every time step, this approach has analytical accuracy (only affected by temporal discretization) and just solves for the surface temperature. The drive-cycle results indicated a reduction in heat transfer, an increase in exhaust enthalpy, and simultaneously a fuel mass savings.

The structural integrity of thermal barrier coatings has been a challenge that has limited their widespread adoption in engines, and reports of failures are prevalent in the literature.[44–50] Rapid heating and cooling of the surface leads to coating delamination (debonding). Optimizing solely for heat transfer may result in impractical coating materials and thicknesses. A detailed discussion of such an unconstrained optimization is included below. Consequently, the durability characteristics of coatings should be considered when performing material or thickness optimization. This study employs a methodology to evaluate coatings' durability due to thermomechanical loading. A brief overview of the durability mechanics technique is given below and further details can be found in Koutsakis et al.[51,52] This coating delamination framework was employed to predict the delamination of several thermal-barrier-coated pistons that had been tested in a high-output, single-cylinder diesel engine.[53] The on-engine coating durability observations and model results were consistent, verifying this methodology.

A major concern for exhaust aftertreatment is the transient thermal behavior of catalytic devices during cold start operation.[54–56] Recently, the effect of adiabatic thermal insulation on various aftertreatments components has been demonstrated over a WLTC (Worldwide harmonized Light vehicles Test Cycle). In this study, were no improvements in fuel consumption, however, the adiabatic insulation increased the exhaust enthalpy and lowered the cumulative pollutant emissions.[57] This behavior can be explained by the complicated non-linear coupling between the multiple effects at play. In order to eliminate this behavior and provide a comprehensive comparison between a coated and an uncoated engine a transient drive cycle needs to be considered.

The objective of this paper is to demonstrate an optimization procedure for selecting thermal barrier coatings that includes both thermal and durability performance considerations. Failure to include the durability constraint gives rise to a trivial solution – the best thermal insulation is achieved with the thickest

possible coating. In this work, only the piston surface is considered for coating. The optimization was constrained to choose from a database of existing materials to ensure that a realizable solution was achieved. In addition, a full drive cycle was simulated to minimize the potential bias associated with performing the optimization at one, or just a few operating points. The full procedure involved evaluating the performance for more than one million drive cycles, thus computational efficiency was paramount.

The analysis of the thermal performance was performed using a commercial cycle simulation software package that was modified to include a fully coupled transient wall temperature calculation, which allowed thermal swing coatings to be evaluated.[41,52] A full 20-min drive cycle simulation took approximately 30 h to compute, thus the fully coupled model was not tenable for optimization purposes. The required computational efficiency was realized through the uncoupled application of the thermal and mechanics equations. The validity of this assumption is discussed fully below and was verified a posteriori by running the fully coupled model for the top 10 coating materials identified through the toughness-constrained optimization.

System-level model setup

A complete system-level simulation model (GT-Power) of the John Deere 4045 engine was used, see Table 1 for the engine specifications. The model can predict steady-state or transient cycles. The transient cycle exercised was the Non-Road Transient Cycle (NRTC).[41,58] All major subsystems in this model either used bench data or were calibrated, including the head flow, EGR valve, exhaust throttle, turbocharger, wastegate, fuel rate of injection profiles, and combustion parameters. Input settings were extracted from the production ECU calibration, and include fuel injection scheduling, rail pressure, air system actuator positions, and other boundary conditions applicable to the 4045 engine. The calibrated model was provided by Deere (Miles S., personal communication, 2020).

The convective in-cylinder heat transfer to the wall is calculated as

$$\dot{q}'' = h\left(t_{\text{gas}} - t_{\text{o, wall}}\right) \tag{1}$$

where h is the heat transfer coefficient from the classical Woschni correlation with the swirl term,[59] t_{gas} is the bulk gas temperature from the gas-phase thermodynamics solver, and t_{wall} is the coated wall temperature. The unsteady conduction within the solid (multi-layer coated) wall was calculated with an updated version of the method used in the initial work of Koutsakis et al.[60,61] Triangular input pulses are used as compared to step pulses of heat flux, which gives higher accuracy. This analytical technique calculates the wall temperature only at the combustion surface "node" as opposed to finite difference schemes that have to compute the

Table 1. John Deere 4045HFC04 engine geometry.

Number of cylinders	4
Displacement volume	4.5 L
Stroke	127 mm
Bore	106.5 mm
Connecting rod	203 mm
Compression ratio	17.0:1
Firing order	1-3-4-2

temperature at every single node, and this solution is exact (except for temporal discretization) whereas finite difference methods require high node density (and computational time) to achieve accuracy. The mathematical solution relies on complex analysis to invert the Laplace transform of surface temperature from the frequency domain back to the time domain. The time-response functions, X_o and Y_o, which describe the multi-layer conduction physics, only need to be calculated once before the simulation initiates. The X_o response refers to the surface temperature rise due to an input heat flux $\dot{q}''$ at the combustion surface while the Y_o response refers to the surface temperature rise due to a temperature change of the back-side coolant/oil surface, t_N. The surface temperature can be shown to be the convolution of the previous heat flux or coolant/oil temperature with the respective response function. The superposition of the two subproblems provides the instantaneous wall surface temperature $t_{\text{o, wall}}$ for a multilayer as:

$$t_{\text{o, wall}}[n] = (X_o \circledast \dot{q}'')[n] + (Y_o \circledast t_N)[n] \tag{2}$$

where $\circledast$ denotes convolution. Additional details about the conduction heat transfer methodology can be found in Koutsakis et al.[41,42,52]

Uncoupled thermo-mechanical analysis

Decoupling the heat transfer calculation from the full powertrain model, that is, using the uncoated piston heat flux from the full model for coated piston simulation, can significantly reduce the computational effort to optimize a piston thermal barrier coating. However, this requires assumptions about gas temperature and engine breathing. The validity of these assumptions is discussed below.

Baseline gas temperature assumption

If one assumes that the combustion gas temperature and the heat transfer coefficient are minimally affected by the presence of the coating, one can take h and t_{gas} from the fully coupled baseline solution and independently compute $t_{\text{o, wall}}$, from which an updated wall heat flux can be determined. After just a few iterations, in practice, a converged wall temperature solution is achieved. The wall temperature drives the mechanical

Table 2. Thermo-mechanical properties of wall architectures investigated, with k: thermal conductivity, ρ: density, c: specific heat capacity, L: thickness, E: Young's modulus α: coefficient of thermal expansion, ν: Poisson ratio, t_{ref}: stress-free temperature and G_c: toughness.

Material	k [W/m-K]	ρ [kg/m^3]	c [J/kg-K]	L [μ m]	E [GPa]	α [ppm K^{-1}]	ν [-]	t_{ref} [K]	G_c [J/m^2]
8YSZ + Polyester[63]	0.42	4473	358	300	20	11.5	0.33	473	40
Stock Al Piston	123	2702	949	8300	75	21	0.33	473	–

response without any feedback so the mechanical response can be solved after thermal convergence. This, however, requires that the gas temperature is not significantly affected by the change in heat loss due to the coating; the constant h assumption arises from an incomplete understanding of coating roughness effects.[9,28–31,33,62]

Figure 1 shows a comparison of the fully coupled baseline (uncoated) case to the fully coupled coated case, and the uncoupled coated results. The data are for a steady-state cycle of the production John Deere 4045 engine. The load was held fixed at 10.9 bar IMEPg load by adjusting the fuel mass injected and engine speed was 800 rpm. The stock piston material was used for the baseline uncoated case; a modern, low-volumetric-heat-capacity coating was used on top of the aluminum wall for the coupled and uncoupled coated cases. Material thermal properties of the engine wall architecture can be found in Table 2. The baseline wall thickness was 8.6 mm.

The gas and piston temperature are shown in Figure 1(a) as a function of crank-angle. The coupled gas temperature solutions for the baseline and coated case are seen to match very well, which is a necessary but not sufficient condition because ultimately it is the heat transfer estimation that matters. The baseline uncoated wall surface temperature showed negligible temperature swing, as expected. The coupled coated case, which uses the simultaneously solved gas temperature, shows a significant temperature swing. The uncoupled coated piston temperature, which uses h and t_{gas} from the baseline calculation, also shows a significant swing, and the cycle-mean magnitude of the swing is seen to be almost 2.5% higher than for the coupled case.

The piston heat flux is shown in Figure 1(b) for the two coated cases. Recall, the uncoupled case uses the baseline uncoated gas temperature and heat transfer coefficient. It can be seen that there is quite good agreement between coupled and uncoupled piston heat flux, that is, the slightly higher uncoupled gas temperature partially compensates for the slightly higher piston temperature.

The ultimate comparison, however, is to assess the uncoupled gas temperature assumption on the *total* heat transfer rate. The total heat transfer difference is suppressed because the cylinder head and liner heat transfer rates, which are minimally affected, are
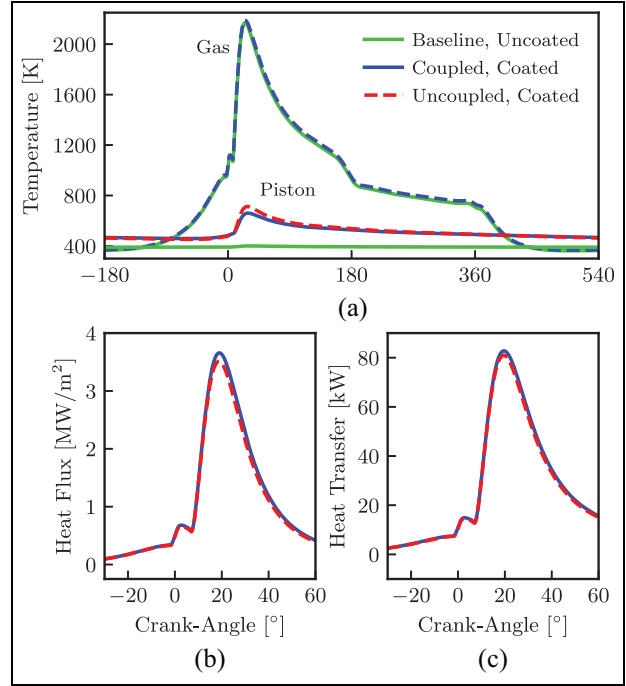

Figure 1. (a) Gas/wall temperatures and (b) instantaneous *piston* heat flux and (c) *total* heat transfer rates for a baseline aluminum and coupled/uncoupled case of a thermal swing coating. The total heat transfer percentage error between the coupled and uncoupled coated approach is 0.27%.

included in the calculation. The total heat transfer rate, $\dot{q}_{total}$, shown in Figure 1(c), is given by

$$\dot{q}_{total}(\theta) = \dot{q}''_{head}(\theta)A_{head} \\ + \dot{q}''_{piston}(\theta)A_{piston} \\ + \dot{q}''_{liner}(\theta)A_{liner}(\theta) \tag{3}$$

where $\dot{q}''_{head}$, $\dot{q}''_{piston}$ and $\dot{q}''_{liner}$ are the head, piston and liner heat flux, respectively, and the terms A_{head}, A_{piston}, and A_{liner} are the corresponding surface areas; the liner area varies with crank angle. For this operating condition, the percentage error between the uncoupled and coupled *total* heat transfer rate was 0.27%.

The *coupled* solution requires evaluation of a direct form convolution *at each time step*, see equation (2); the current wall temperature is calculated based on the convolution of previous and current heat flux arrays and the wall response function.

The *uncoupled* solution, however, can be solved with a *single* convolution, which can be sped up significantly using the Fourier-domain properties of the convolution.

$$t_o = X_o \circledast \dot{q}'' = \mathcal{F}^{-1}\{\mathcal{F}\{X_o\} \cdot \mathcal{F}\{\dot{q}''\}\} \quad (4)$$

where $\dot{q}''$ is the full heat flux history, which is known since t_g, t_o, and h are known for the full duration of interest. The symbols $\mathcal{F}$ and $\mathcal{F}^{-1}$ denote Fourier transform to the frequency and time domain, respectively. As discussed above, an iterative solution, where t_o is updated for each iteration, is required. Convergence was achieved in only a few iterations.

The *uncoupled* problem could also be resolved with a finite difference approach, but that would incur significant computational cost. Each spatial node of the computation domain would have to be calculated (and iterated) for all the $\sim 2^{24}$ time steps of the transient drive cycle. On the contrary, large heat flux histories can very efficiently be handled in the frequency domain[61] with the current analytical conduction technique. To maximize computational efficiency, convolution techniques such as the Overlap-Add can be employed, using the very long signal as the heat flux $\dot{q}''$ and the finite-impulse-response filter as the response function X_o.[64]

According to all the above, the use of baseline gas temperature and heat transfer coefficient data to investigate TBC performance appears to be a reasonable assumption for this piston coating optimization study.

Baseline engine breathing assumption

One limitation of thermally insulated engines has historically been the reduction of volumetric efficiency due to the flow of heat from the wall to the gas during the intake stroke. A significant amount of heat transfer during the intake stroke could limit the applicability of an uncoupled approach. Morel et al.[65] defined the term "pumped heat" per unit area as

$$q''_{pumped} = \frac{1}{2}\left[\oint |\dot{q}''| \, d\theta - \oint \dot{q}'' \, d\theta\right] \quad (5)$$

which represents the amount of heat flux from the wall to the gas; the wall temperature is practically only higher than the gas temperature during the intake stroke. The integration is performed over a full engine cycle, hence the $\oint$. Thus, the pumped heat provides a useful metric to assess the breathing performance of the engine when it is computationally expensive to calculate the gas flow, and it can be utilized as a surrogate for the volumetric efficiency, that is, the pumped heat is increasing for decreasing volumetric efficiency.

The pumped heat ratio of a piston-coated engine relative to a baseline engine is defined as

$$\Gamma_{pumped} = 100 \times$$
$$\frac{\left[q''_{pumped, piston, coated} - q''_{pumped, piston, uncoated}\right] A_{piston}}{Q''_{pumped, uncoated}}$$
$$(6)$$

where the pumped heat of the baseline engine, $Q''_{pumped, uncoated}$, is defined as

$$Q''_{pumped, uncoated} = q''_{pumped, head} A_{head} + q''_{pumped, piston} A_{piston}$$
$$+ \oint\left(|\dot{q}''_{liner}| - \dot{q}''_{liner}\right) A_{liner} \, d\theta$$
$$(7)$$

In order to assess whether the presence of the coating would affect engine breathing to an extent that an uncoupled solution would be insufficient, fully coupled simulations for the coating given in Table 2 and an expected optimal coating – Silica Aerogel – were performed. Figure 2(a) shows the volumetric efficiency, calculated for each cycle at IVC, as a function of drive cycle time for both coatings compared to the baseline. There was an average reduction of less than 0.5% and 2%, respectively, for the two coatings simulated.

Figure 2(b) correlates the pumped heat ratio, defined in equation (6), with the relative volumetric efficiency change for the two coatings. Each point represents a different cycle. It can be clearly seen that the pumped heat transfer is increasing – more heat is transferred from the wall to the inducted air – when there is a lower volumetric efficiency, but the relationship is not 1:1.

Figure 2(c) shows the mean value of Γ_{pumped} over the full drive cycle compared to the total change of volumetric efficiency for the drive cycle. Additional coatings for which fully coupled simulations are also included. It can be seen that in spite of the modest cycle-by-cycle correlation, over the full drive cycle Γ_{pumped} is a good indicator of breathing penalty.

The engine breathing changes shown above are relatively small, and can be safely neglected when coating performance is estimated using an uncoupled approach.

Computational time comparison

The uncoupled approach was followed for conducting the optimization due to its substantial computational time advantage and its more-than-sufficient accuracy. An example of the elapsed times of each approach is provided for reference. A fully coupled simulation of the engine with the coating given in Table 2 over the NRTC drive cycle time (having a real time of 1258 s. and requiring a total of 2^{24} timesteps) on a modest workstation (Intel-i5 3GHz, 32GB RAM) took 108,188 s or 86× real time. It is to be noted that the primary source of slowdown relative to the uncoated case, that is, 50× real time, was due to communication
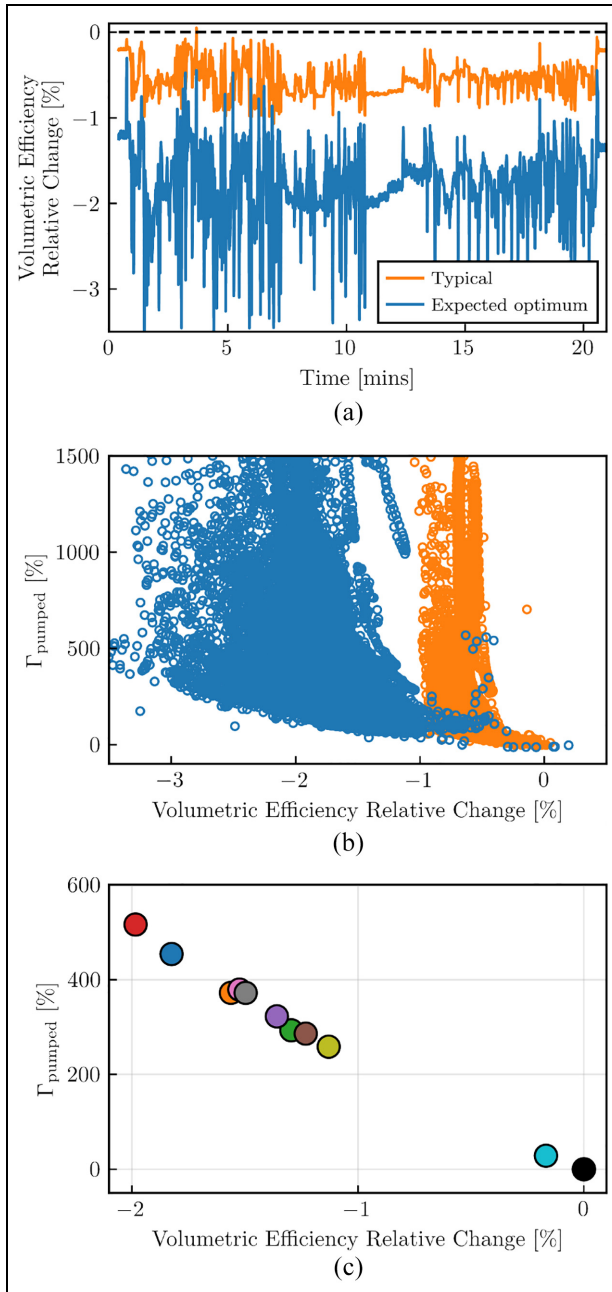
Figure 2. (a) Volumetric efficiency change relative to uncoated baseline as a function of drive cycle time. (b) Pumped heat transfer correlated with the volumetric efficiency on a cycle-by-cycle basis. (c) Drive-cycle-averaged comparison of Γ_{pumped} and volumetric efficiency change for multiple coatings.

between the user-defined function and the main commercial code.[41,66] On the other hand, the uncoupled simulation required only 7.5 s or $0.006\times$ real time. Moreover, the uncoupled method was developed in Python, an open-source language, rather than the coupled simulation which relies on a commercial code. Thus, the uncoupled method could be freely parallelized.

Multilayer mechanics analysis

Propulsion systems and spacecraft reentry vehicles often use protective coatings for components exposed
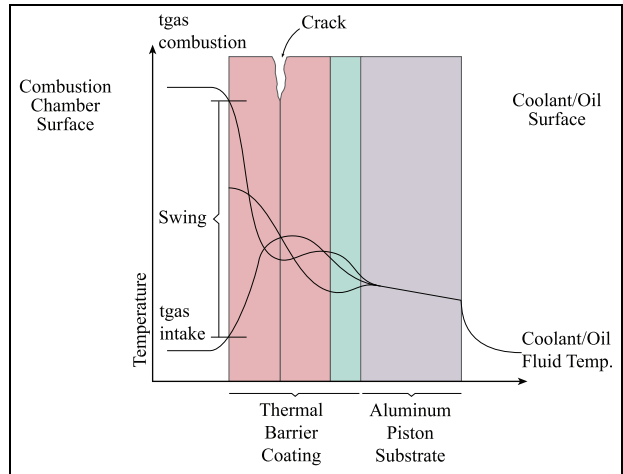
Figure 3. Schematic illustration of a thermal barrier coated aluminum piston wall exposed to combustion chamber gases (left) and coolant/oil (right). The wall temperature distribution is illustrated at various different times during the engine cycle, that is, intake, combustion, mid-expansion. A delamination due to crack propagation is illustrated at the mid-coating region.

to extreme thermal conditions because most structural materials do not exhibit sufficient thermal performance, and vice versa. Multilayer architectures are often employed to balance thermal properties, stored strain energy arising from thermal misfit, and adhesion. A single-layer material that combines equally good thermal and mechanical properties is hard to find. Therefore, the choice of a multilayer architecture is favored.

The release of elastic strain energy stored in the coating, which builds up due to thermal stresses, supplies the main driving force for delamination in thermal barrier coating systems. The method requires the full multilayer wall temperature distribution during an engine cycle for calculation, and depends on mechanical properties such as elastic modulus, coefficient of thermal expansion, and Poisson ratio. Figure 3 shows a thin thermal barrier coating bonded to an aluminum piston substrate. The left surface is exposed to the combustion gases while the right is oil-cooled. The combustion chamber surface temperature may vary anywhere between the intake stroke and combustion extremes, resulting in a wide temperature distribution envelope throughout the engine cycle. The reference or stress-free temperature defines the state at which the multilayer is at a relaxed, stress-free condition. The approach taken is to assume that a crack exists at a specific location in the structure, see Figure 3. The difference in strain energy, U, between the intact structure below the crack in Figure 3 and the two parts separated by the crack was calculated and termed the elastic energy release rate, G

$$G = U^{\text{whole}} - \left(U^{\text{top}} + U^{\text{bottom}} \right) \qquad (8)$$

where U^{whole}, U^{bottom}, and U^{top} are the strain energy of the intact multilayer, piston substrate, and debonded

coating, respectively. The general methodology to calculate the energy release rate and the the equations that estimate each strain energy, which are involved and can not be easily summarized, are given in Koutsakis et al.[51,52]

The hypothesis is that the crack will advance when G exceeds a threshold that depends only on thermomechanical material properties. This critical parameter is the toughness G_c of the material or the interface – it is an experimental measurement, not a calculated parameter. The calculated elastic energy release rate, G, with units of energy/area is a function of specimen geometry, material properties and thermomechanical load. Crack growth is initiated when the energy release rate overcomes toughness, as given in equation (9).

$$G \geqslant G_c \qquad (9)$$

Optimization setup

Mathematical formulation

Thermal insulation can be exploited for various reasons: to increase engine efficiency and power output by decreasing heat rejection and cooling requirements; to provide thermal protection to the underlying power-cylinder components; or to increase exhaust enthalpy for enhancing conversion efficiency of emission after-treatment components.

This work focuses solely on providing in-cylinder heat insulation to maximizing engine efficiency over a large number of material candidates. The objective is met by minimizing the net in-cylinder heat transfer to the piston while ensuring (1) the compression ratio remains fixed, (2) the coating/piston interface temperature is below the metal's maximum service temperature, and (3) the coating has sufficient structural integrity. The above is achieved by optimizing the thickness of each individual material type.

The mathematical formulation of the proposed optimization problem is described as

$$\underset{\text{MatID, L}}{\text{minimize}} \quad w_{net}\Gamma_{net} + w_{pumped}\Gamma_{pumped} \qquad (10a)$$

$$\text{subject to} \qquad w_{net} = 1 - w_{pumped}, \qquad (10b)$$

$$L_{ini} = \sum L_i, \qquad (10c)$$

$$t_{sub-int} \leqslant t_{max, service}, \qquad (10d)$$

$$G \leqslant G_{max, service} \qquad (10e)$$

where the relative net and pumped heat transfer changes, Γ_{net} (defined fully below) and Γ_{pumped}, respectively, are treated as a single objective with corresponding weighting factors w_{net} and w_{pumped}. The design variables are the material type and thickness, termed matID and L, respectively.

It was shown earlier that the volumetric efficiency penalty when optimizing a piston coating for the given drive cycle was quite small. But, in other instances, for example, insulating the full combustion chamber, using other combustion strategies, or optimizing at specific engine conditions, volumetric efficiency losses may be important to consider. Thus, Γ_{pumped} is included in equation (10) although in this work w_{pumped} was taken as zero, which results in simply minimizing Γ_{net}. The full expression for the relative reduction in heat loss, Γ_{net}, is

$$\Gamma_{net} = 100 \times \frac{\left[\int\limits_{\text{Coated}} \dot{q}''_{o, piston} \, d\theta - \int\limits_{\text{Uncoated}} \dot{q}''_{o, piston} \, d\theta \right] A_{piston}}{Q_{o, Uncoated}} \qquad (11)$$

where the numerator is the difference between the energy lost to the piston between coated and uncoated conditions, and the denominator is, with reference to equation (3)

$$Q_{o, Uncoated} = \int\limits_{\text{Uncoated}} \dot{q}_{total}(\theta) \, d\theta \qquad (12)$$

Computational approach

The optimization routine was written in Python using the `scipy.optimize.minimize` function from the SciPy[67] library. The selected minimization algorithm utilized a constrained trust-region method. Termination tolerances were set for the norm of the Lagrangian gradient, the change of independent variable and threshold on the barrier parameters were set as 10^{-10}, 10^{-10}, and 10^{-4}, respectively. A computational node in a cluster would be given the material ID and would optimize coating thickness based on the given constraints. A demonstration of the full computational process will be given using the wall architecture from Table 2 for a 300 μm thickness. First, the heat transfer solution will be discussed followed by the mechanics analysis.

Baseline, uncoated boundary conditions of the full drive cycle are imported, that is, time, heat transfer coefficient, gas temperature, uncoated heat flux (so that it only is calculated once) and the piston under-side temperature, which was computed using a detailed analysis in GT-Power. The coating thickness, set by the optimizer, is used to calculate the piston thickness based on the equality constraint (10c). The thermal properties, such as thermal conductivity k, specific heat capacity c and density ρ, of the coating material are imported from the materials library and the thermal resistance $R = L/k$ per unit area and capacitance per unit area $C = \rho c L$ are calculated for each layer; these parameters are required for the evaluation of X_o and Y_o. Once the wall functions X_o and Y_o are found, the wall surface temperature is determined using equation (2), and the process is iterated until a convergence criterion of 0.1% RMS error of peak surface heat flux was met. The metal/coating interface temperature history was calculated in a similar manner, but with slightly different wall functions, X_i and Y_i, see Koutsakis and
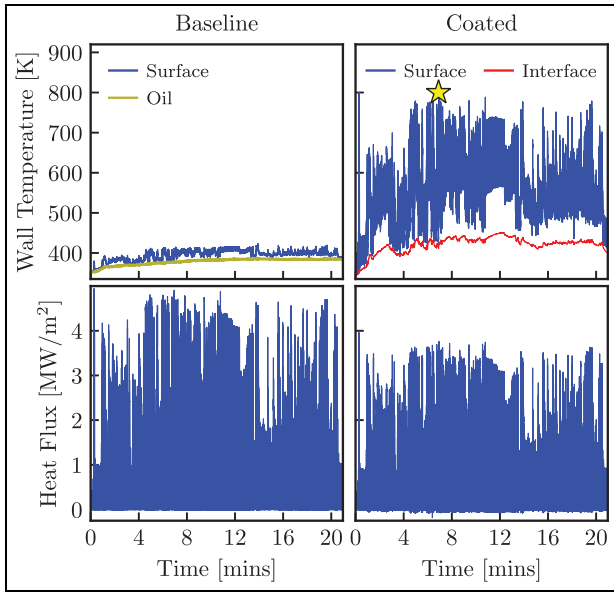
Figure 4. Wall temperature (top) and heat flux (bottom) temporal evolution of the baseline and a coated case during the drive cycle.

Ghandhi[42] for details. It is worth noting that the wall surface and interface temperatures are evaluated with a single convolution. The maximum interface temperature over the drive cycle was found, and compared against the maximum service temperature of the aluminum substrate, 643 K (370°C), per constraint (10d).

Figure 4 shows the wall surface temperature (top) and heat flux (bottom) for the baseline and sample coated case over the drive cycle time. The interface temperature of the coated case, shown with red, satisfies the inequality constraint (10d). During the early part of the drive cycle the surface temperatures are increasing due to wall heating. The surface temperature for the coated case is significantly higher than for the baseline, which in turn gives significantly lower heat flux.

The coated piston heat flux allows one to evaluate the integrated net and pumped heat transfer rates over the drive cycle. The total (all four pistons) surface area was $A_{piston} = 0.011937$ m^2, giving the integrals of uncoated and coated piston net heat transfer of $\int_{Uncoated} \dot{q}''_{o,\,piston} A_{piston} \mathrm{d}\theta = 11.8$ MJ and $\int_{Coated} \dot{q}''_{o,\,piston} A_{piston} \mathrm{d}\theta = 8.8$ MJ. The total (head + piston + liner) net heat transfer of the baseline coupled case was imported from GT-Power, $Q_{o,\,Uncoated} = 30.35$ MJ. These values give $\Gamma_{net} = -9.7\%$, that is, nearly a 10% reduction in cylinder wall heat transfer. Following a similar procedure, one finds the relative pumped heat transfer change as $\Gamma_{pumped} = 320\%$.

The durability analysis is the last step before the optimizer decides whether or not this solution is feasible. The mechanics model described earlier[51] is called separately because it is too computationally expensive to run at every time step. For all of the conditions tested, the maximum energy release rate was found to occur on the cycle that had the highest surface temperature (other criteria tested included cycles with the highest heat flux, highest temperature difference between combustion and oil surface, and highest interface temperature). Additionally, previous results indicated[51] that the peak energy release rate was found to occur later in the cycle than the peak surface temperature. Delamination was often located within the coating as compared to at the coating-substrate interface where there was a mismatch in coefficient of thermal expansion, or at the coating surface where the stress was maximum. Such a failure mechanism has been experimentally demonstrated in the modern reciprocating coating literature.[50] Thus, the mechanics analysis was only performed for the central location of the coating during the expansion stroke for the highest piston surface temperature cycle.

The mechanics model discretizes the wall into a finite number of individual layers. Thus, the temperature distribution within the wall is necessary. The analytical method could be used to solve for the entire wall distribution, but that would not be efficient; the main computational advantage is that it only solves at specific locations, for example, the combustion chamber surface.

Figure 5 illustrates the procedure to estimate the highest energy release rate in the drive cycle, as described above. The time of the maximum wall surface temperature was found. For this example, this occurs shortly after the 416th second, as shown in Figure 5(a). A Crank-Nicolson finite difference heat transfer model was used to find the wall temperature distribution. In order to correctly match the initial conditions on the cycle of interest, the finite difference code was started 30 cycles prior to the hottest expansion stroke. An initial condition – based on the analytically derived surface heat flux up to that point of time – was provided to the numerical model. The two methods converge after a few cycles, as can be seen from the absolute difference curve in Figure 5(a) (dotted black). The spatial domain, comprised of the coating and the piston substrate wall, was linearly discretized with 2^6 and 2^4 nodes, respectively.

The wall temperature distribution was imported together with all the thermomechanical properties into the mechanics model to calculate the energy release rate at the mid-coating (green) and coating/piston interface (magenta) locations, see Figure 5(b). The mechanics model used the same grid spacing as the finite difference heat transfer model. The energy release rate (both at the center and the interface) increases for increasing surface temperature. Figure 5(b) is shown for demonstration purposes only. The actual time period that the mechanics model was enabled during the optimization was from the crank-angle location of the maximum wall surface temperature until the BDC of that cycle. Results for this time period are shown in Figure 5(c). As the surface temperature decreases, starting from its
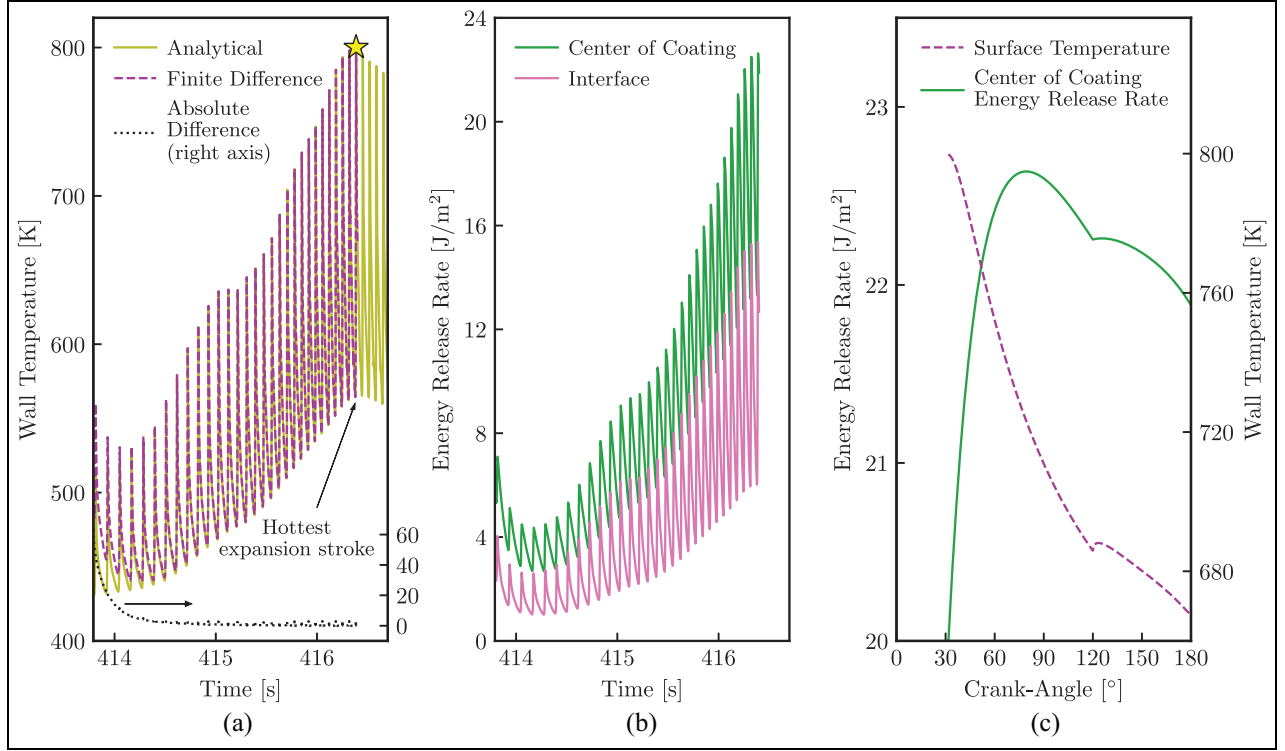
Figure 5. (a) Wall surface temperature comparison between the analytical and finite difference method as a function of time prior to the hottest expansion stroke. The yellow star highlights the time of maximum surface temperature in the drive cycle. (b) Mid-coating and interface energy release rate temporal evolution. (c) Surface temperature and mid-coating energy release rate.
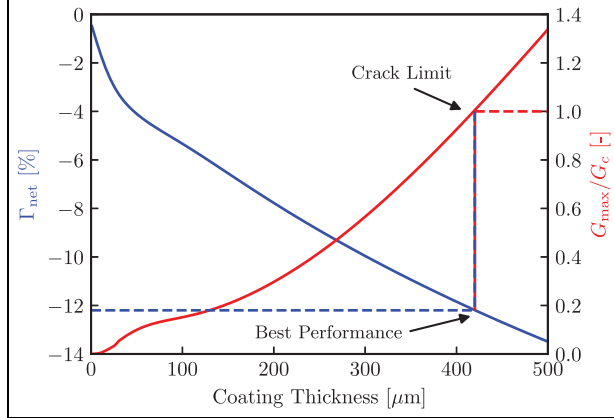

Figure 6. Trade-off between in-cylinder heat transfer reduction and maximum energy release rate for various coating thicknesses. Wall architecture thermomechanical properties can be found in Table 2.

maximum at about 30° aTDC, the energy release rate at the mid-coating location increases rapidly until reaching a peak at about 80° aTDC.

The maximum energy release rate is stored and used in the inequality constraint (10e). If the constraint is violated, the solution becomes non-feasible and the optimization solver attempts to reduce coating thickness until the constraint is satisfied.

Figure 6 depicts the trade-off between in-cylinder heat transfer, Γ_{net}, and G_{max}/G_c. The former is heat transfer reduction, per equation (11), while the latter is the ratio of maximum energy release rate and the material toughness. The results shown are derived based on the full drive cycle. As the coating thickness increases the heat transfer decreases but G_{max}/G_c increases rapidly, indicating the likelihood of a coating failure. The optimizer is minimizing the heat transfer according to the path defined by the dashed lines depicted in Figure 6; it increases the thickness to get the "Best Performance" until reaching $G_{max}/G_c = 1$, which is defined as "Crack Limit."

Distributed parallelization via high-throughput computing

The procedure described above was conducted to optimize the thickness of a single material. Both the material type and thickness were used as design variables in the optimization problem. This hierarchical-type optimization was performed in parallel. The parallel mode was run using the HTCondor scheduling software,[68] which offered access to a pool of 2000–6000 execution nodes concurrently. A job was created for each material type and the jobs were and distributed to all the "workers" around the pool. Each worker optimized the

Table 3. Optimization Specifications.

Number of cycles	20,000
Number of materials	800
Stress-free temperature	473 K (200°C)
Maximum substrate temperature	643 K (370°C)
Lower/upper coating thickness bound	0/500 μm
Maximum mid-coating energy release rate	Parameterized*

*Five optimization scenarios were conducted: unconstrained, 10, 50,and 100 J/m² and individual material's toughness.

Figure 7. In-cylinder heat transfer reduction relative to the baseline, Γ_{net}, classified by material family (ceramics, glasses, metals and polymers) for the mechanical constraints at 10, 50, and 100 J/m², and the unconstrained case.

thickness of the given material. A large set of data were provided back to the master computer containing function outputs of every evaluation including the optimum. A comprehensive list of the main optimization characteristics is provided in Table 3.

The hierarchical optimization – with material type and thickness as design variables – was performed five times in total to demonstrate how the coating's structural integrity affects engine heat transfer performance. The scenarios were: mechanically unconstrained, mechanically constrained by energy release rate (three levels of constraint: 10, 50, and 100 J/m²), and mechanically constrained by the toughness of each individual material.

Materials library

An in-house materials property library was developed from thermomechanical properties found in the literature. The majority of the properties were collected from ANSYS Granta Selector,[69] a commercially available database. All material families were included as long as they satisfied an initial-stage filtering. The data were filtered such that they had a thermal conductivity and maximum service temperature less than 30 W/m-K and greater than 500 K, respectively. This filtering process resulted in 781 potential materials. Another 15 thermal protection system (TPS) materials were also included from the TPSX library.[70] Unfortunately, the modern engine literature has limited thermomechanical property data. Nonetheless, a few extra materials were included based on experimentally measured data[27,31,63] via private communication with the authors.

The in-house library contained a number of 800 materials. The data included the matID, material name, material family (ceramic, glass, metal, and polymer) thermal conductivity, density, specific heat capacity, Young's elastic modulus, Poisson ratio, and toughness.

Figure A1, shown in the Appendix, depicts the thermomechanical properties used in this optimization study. Figure A1(a) shows the thermal conductivity versus volumetric heat capacity. Coatings with low thermal conductivity and low volumetric heat capacity have garnered recent interest. Several of the ceramic and glass materials satisfy these criteria, which is primarily achieved with high levels of porosity, for example, aerogels and foams. The metals have the highest
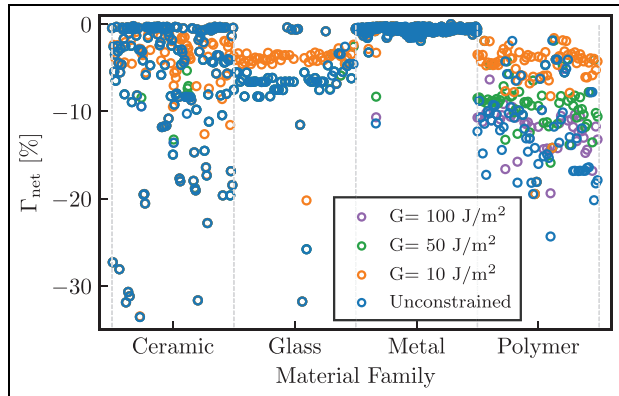
conductance and volumetric heat capacities. Polymers tend to have lower thermal conductivity, by at least one order of magnitude, but comparable volumetric heat capacity to that of metals.

Figure A1(b) shows the coefficient of thermal expansion (CTE) against thermal conductivity. Polymers tend to have the highest CTE. Figure A1(c) shows that the Young's modulus is a strong function of density. Figure A1(d) shows toughness (or fracture energy) as a function of material density. Toughness is the ability of a material to absorb energy without fracturing with units of energy per unit area. Metals and polymers have the highest toughness, whereas ceramics and glasses are brittle materials and prone to failure. However, recall that the relevant issue is the energy release rate relative to toughness, not the toughness alone.

The material families that show attractive thermal properties, per Figure A1(a), are the ones that tend to have undesirable mechanical properties, per Figure A1(d). This trade-off is the reason why real materials were chosen for this study. An optimization based on just thermal properties can result in an unobtainable solution.

Optimization results

Multiple optimization scenarios were performed, see Table 3. The rationale was based on the fact that the actual material properties of the *as-sprayed* coatings are manufacturing-process-dependent. The vast majority of the in-house material property library, discussed above, contained properties of bulk materials.

Engine heat transfer performance

Figures 7 to 12, discussed together below, represent the optimization results. Figures 7 and 9 show optimal heat transfer reduction relative to the baseline for each
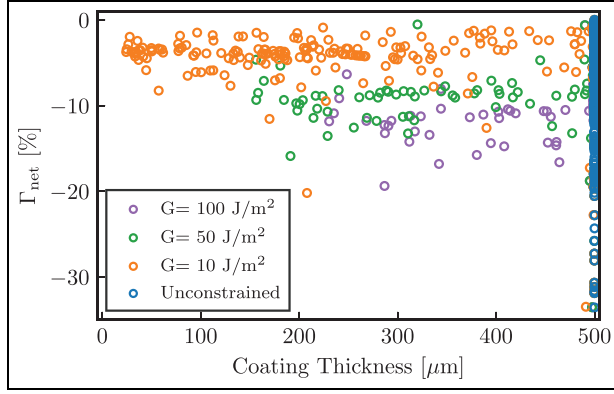
Figure 8. In-cylinder heat transfer reduction relative to the baseline, Γ_{net}, as a function of the optimum coating thickness for mechanically constrained cases.
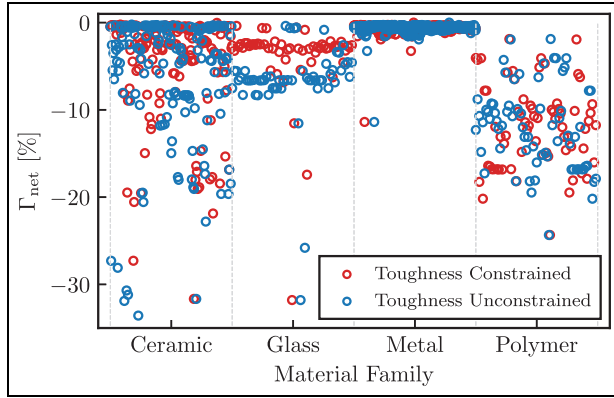

Figure 9. In-cylinder heat transfer reduction relative to the baseline, Γ_{net}, classified by material family (ceramics, glasses, metals, and polymers) for the mechanically constrained by individual's material toughness case.
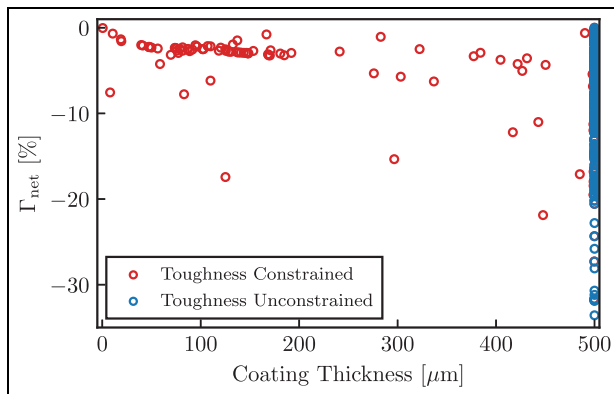

Figure 10. In-cylinder heat transfer reduction relative to the baseline, Γ_{net}, as a function of the optimum coating thickness for the toughness-constrained cases.

Figure 11. Comparison of the constrained versus the unconstrained in-cylinder heat transfer reduction for both mechanically constraints optimization scenarios.

matID categorized by the material family: ceramics, glasses, metals, and polymers. Figures 8 and 10 show the mechanically constrained results at three levels of constraint: 10, 50, and 100 J/m^2, and the optimal results constrained by the individual material's toughness, respectively. All the above figures include the unconstrained optimization as reference since it is the best thermal insulation achieved, that is, the thickest possible coating. Each data point represents the optimum for a given matID and toughness constraint. Figure 11 directly compares Γ_{net} between the unconstrained and constrained cases.

As expected, a number of the ceramics and glasses provide high heat transfer reduction, see Figures 7 and 9. Almost all the ceramics with Γ_{net} lower than -10% were not penalized from the energy release rate constraints, see Figures 7 and 11. Surprisingly, some of the materials did get penalized for the toughness-constrained case, as shown in Figure 9. Polymers seem to perform quite well; however, the dependence of heat transfer reduction on the mechanical constraint is much more apparent, that is, the polymer optimal points are reasonably more distributed than the other material families in Figure 7.

The optimal thickness of the unconstrained optimization is 500 μm, see Figures 8 and 10. Many optimal thickness values are below the upper bound in Figures 8 and 10. In Figure 8 as the maximum energy release rate limit is reduced the number of cases constrained grows. In addition, the optimal thicknesses of the toughness-constrained case is more distributed along the thickness range, see Figure 10. The distribution of thickness optima is discussed below.

The effect of the energy release rate constraint on the optima can be more clearly illustrated in Figure 11. The constrained versus the unconstrained Γ_{net} are compared for all the optimization scenarios described above. The vast majority of the solutions lie on the 1:1 line,
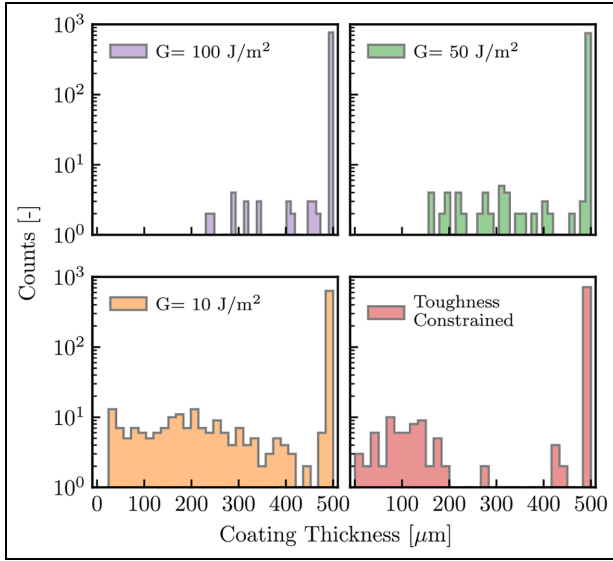
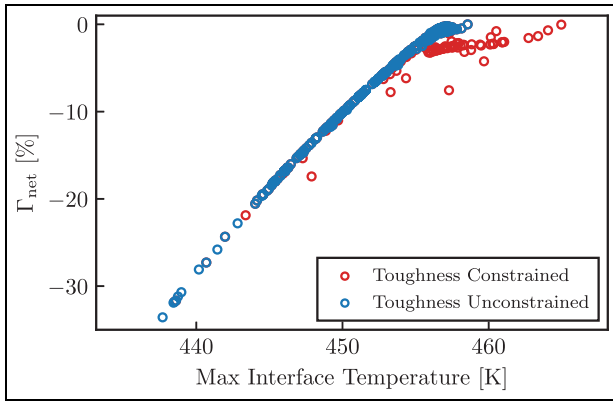**Figure 12.** Histograms of optimal coating thickness for mechanically constrained optimization scenarios.

Figure 13. Comparison of Γ_{net} with the maximum drive cycle interface temperature for the mechanically constrained by individual's material toughness case (red) and the unconstrained (blue) case.
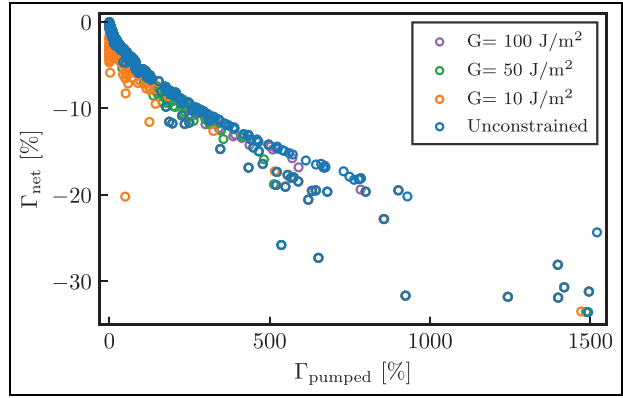

Figure 14. Trade-off between net and pumped in-cylinder heat transfer reduction relative to the baseline.
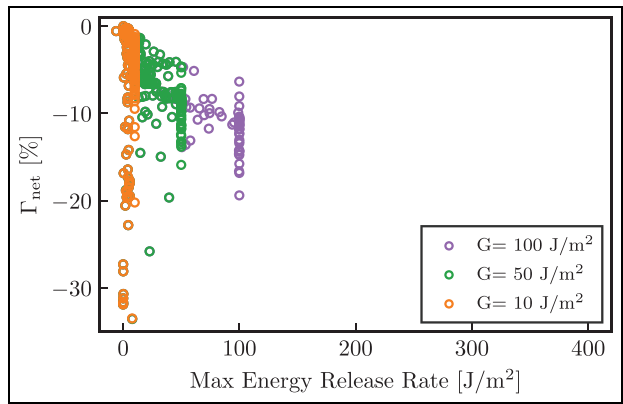

Figure 15. Comparison of Γ_{net} with the maximum energy release rate at the mid-coating location for the mechanically constrained by the three energy release rate levels.

indicating that these materials were not constrained mechanically or via the interface temperature limit. However, every point that lies above the 1:1 line has been forced to reduce its coating thickness, therefore the heat transfer reduction was lower.

The optimal thickness is illustrated using histograms in Figure 12. The vertical axes of all figures represent the number of counts in a bin that spans thickness; 30 bins were used. The unconstrained case has been removed. In Figure 12, it can be seen that the lowest constraint level case ($10 \, \text{J/m}^2$) provides the most distributed optimal thickness distribution relative to the other constraints (50 and $100 \, \text{J/m}^2$). The toughness-constrained optimization also shows high non-uniformity. While the majority of the cases are unaffected, a substantial number of solutions fall in the $0–200 \, \mu\text{m}$ range. It is worth highlighting that this optimization scenario results

in some coatings with almost zero thickness, that is, they could not handle the thermomechanical loading.

Figure 13 shows Γ_{net} with respect to the maximum interface temperature during the drive cycle. It should be noted that the range of maximum interface temperature observed for all candidate materials and optimization scenarios was far below the $643 \, \text{K}$ ($370 \, ^{\circ}\text{C}$) limit defined in Table 3. The maximum interface temperature seen was about $473 \, \text{K}$ ($200 \, ^{\circ}\text{C}$), indicating that optima solutions were not penalized from this constraint. The one-to-one relation between the interface temperature and Γ_{net} is easily explained using the heat transfer resistance analogy; the metal piston is effectively at steady state, and the back-side temperature was specified. Including a convective boundary condition could affect the results in Figure 13, but it is not expected to affect the ranking of coating materials.

Figure 14 illustrates the trade-off between the engine thermal performance benefit, Γ_{net}, and the engine breathing losses, Γ_{pumped}, when a thermal barrier coating is deposited on the piston surface, see Figure 2. Figure 14 shows that Γ_{net} decreases as Γ_{pumped} increases, as expected. Higher in-cylinder heat transfer reduction is accompanied with decreased volumetric efficiency.
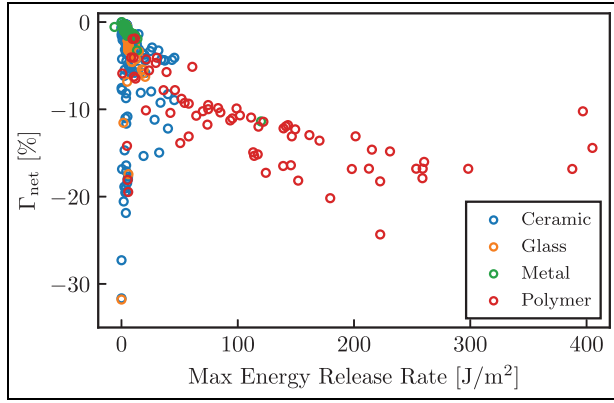
Figure 16. Comparison of Γ_{net} with the maximum energy release rate at the mid-coating location for the mechanically constrained by the toughness of each material candidate grouped by material family.
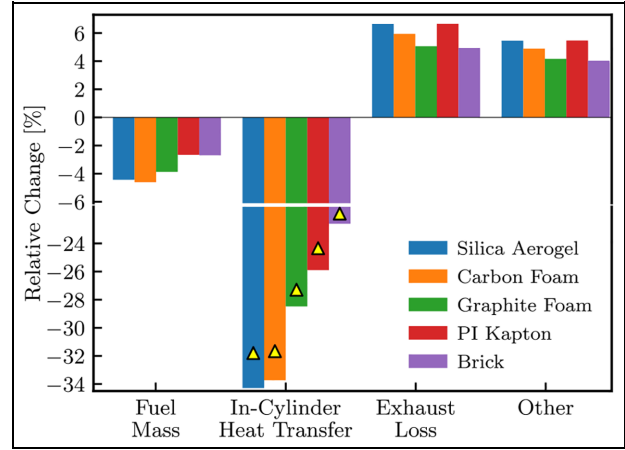

Figure 17. Relative changes of fuel mass and cumulative drive cycle energies for the top 5 piston coatings. The yellow triangles indicate the uncoupled toughness-constrained Γ_{net}.

The differences between the different optimization scenarios are negligible. It is worth noting that in this study the Γ_{pumped} values were simply recorded when the optimum thickness and Γ_{net} were found. In situations where breathing losses are significant, Γ_{pumped} may be included in a single objective function as in equation (10a) or as a bi-objective optimization.

Mechanical performance

Figures 15 and 16 show optimal results of the heat transfer reduction as a function of the maximum energy release rate. In Figure 15, the maximum energy release rate is limited by the corresponding level of constraint (10, 50, and $100 \, J/m^2$), while in Figure 16, the maximum energy release rate is limited by the toughness of each individual material candidate. The toughness constraint not only allowed the maximum energy release rates to increase substantially (up to $400 \, J/m^2$), but penalized cases that would have provided exceptional thermal performance but lacked structural integrity.

Coupled engine simulations using best-performing coatings

The performance of the best coatings identified in the optimization was verified by running the coatings in the fully coupled model. This also allows an *a posteriori* assessment of the uncoupled approach.

Table 4 shows the top 10 materials of the uncoupled toughness-constrained optimization ordered by Γ_{net}. Each row represents a material, and the columns contain performance data. As expected, the metals do not appear in this list due to their high density and conductivity, even though they have the highest toughness, see Figure A1(a) and (d). While it was expected that the majority of the best-performing materials would be ceramics, three polymers feature in the list, with PI Kapton not only performing well mechanically, but also had good thermal performance. In general, the problem with polymeric materials is their ability to withstand high temperature. It is to be noted that one

Table 4. Top 10 materials with the corresponding outputs are shown for the mechanically constrained by toughness optimization.

Material	Γ_{net} [%]	Thickness [μm]	Max ERR [J/m²]	Toughness [J/m²]	Material family [–]
Silica Aerogel	−31.8	500	0.0033	0.313	Glass
Carbon foam	−31.7	500	0.03	61.5	Ceramic
Graphite foam	−27.3	500	0.03	134	Ceramic
PI Kapton	−24.3	500	222	5790	Polymer
Brick	−21.9	448	3.767	3.77	Ceramic
Mullite foam	−20.6	500	1.88	7.75	Ceramic
PEEK (30% Glass fiber)	−20.2	500	179	4340	Polymer
Perfluoro elastomer (FFKM)	−19.5	500	5.7	17,000	Polymer
Zirconia magnesia foam	−19.1	500	3.5	11.4	Ceramic
Zirconia calcia foam	−18.9	500	2.4	15.5	Ceramic

glass, Silica Aerogel, which was imported to the in-house library from TPSX,[70] appears in Table 4. The maximum energy release rate for all of these materials, except brick, were significantly below the toughness constraint.

The material ranking for the other mechanical constraints were different. For example, Glass Foam $(0.13)^{69}$ provided the best thermal performance with a Γ_{net} of almost 33.5%, see Figure 7. However, its very low toughness limited the toughness-constrained Γ_{net} to 7.5% and a thickness of just 8 μm.

Figure 17 shows the relative changes in integrated fuel mass, in-cylinder heat transfer, exhaust loss, and other losses obtained from the fully coupled simulation for the top five materials. The term "Other" is attributed to any other energy pathway, for example, heat transfer to EGR cooler, charge air cooler, heat rejection to coolant/oil in the cylinder head, and heat transfer to surroundings from the block/manifolds/turbine/pipes. For further details on how the cumulative energies are defined, see Koutsakis et al.[41]

Note that the brake power remained fixed for all the cases modeled. First, it is important to highlight that the heat transfer results of the uncoupled and the coupled simulations, the latter shown as yellow triangles, are internally consistent with the materials rankings, which provides confidence that the aforementioned assumptions are valid.

The Silica Aerogel provided the maximum heat transfer reduction, almost 34.3%, but the Carbon Foam provided a slightly larger fuel mass savings, almost 4.6%, which is approximately 150 g over the drive cycle. The fuel consumption benefit is accompanied by an increase in exhaust losses. It is worth noting that PI Kapton resulted in slightly higher exhaust loss than the Silica Aerogel, even though their thermomechanical properties and thermodynamic engine performance were significantly different. The increase of exhaust losses may be advantageous for after-treatment strategies.

The PI Kapton and Brick gave equal fuel savings, however, PI Kapton performs better in terms of heat transfer reduction and exhaust losses. The exhaust losses and other losses strongly correlate.

Figure 18 compares some thermodynamic parameters with the Brake Specific Fuel Consumption (BSFC) for the top 10 coatings. The data are represented as changes relative to the baseline, shown as the black dot. Figure 18(a) shows that Γ_{net} correlates directly with BSFC.

Figure 18(b) shows that the drive-cycle-mean turbine outlet temperature, $t_{turb,out} - t_{turb,out,base}$, is increased for decreasing BSFC. The thermal energy saved cannot be fully converted into brake work; a significant portion ends up as exhaust enthalpy. This temperature difference is directly proportional to the exhaust enthalpy relative losses shown earlier in Figure 17. Using Silica Aerogel coating, the turbine outlet temperature can be increased, by almost 20 K over the drive cycle, which is
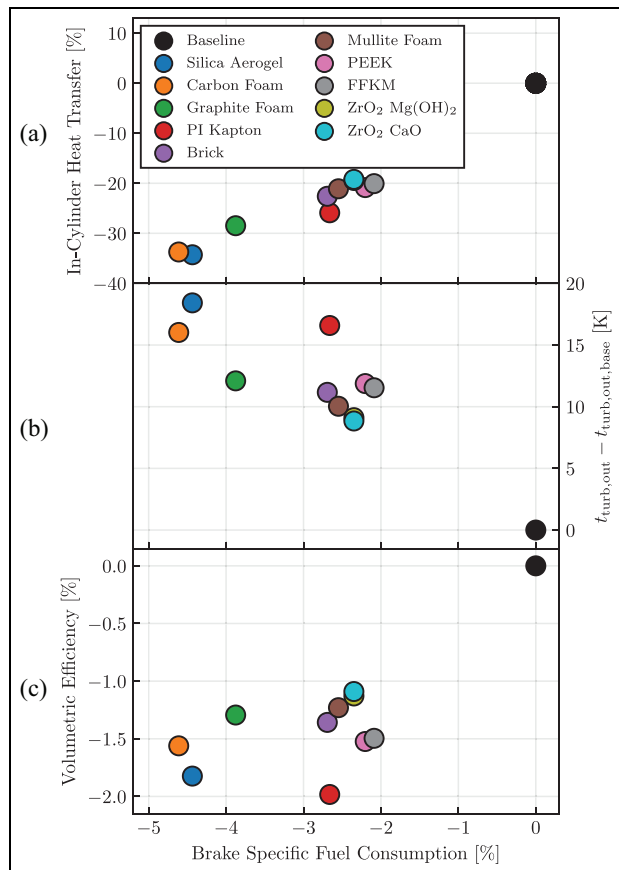

Figure 18. Comparison of (a) in-cylinder heat transfer, (b) drive-cycle-mean turbine outlet temperature, and (c) drive-cycle-mean volumetric efficiency with the brake specific fuel consumption. All data are relative to the baseline.

significant considering that it occurs simultaneously with an almost 4.5% fuel mass saving. Finally, Figure 18(c) shows the volumetric efficiency penalties. In general, the correlation of the volumetric efficiency with the BSFC is not as linear as the previous metrics. Surprisingly, the PI Kapton, which has modest heat transfer benefits among the top-ten coatings, had the highest volumetric efficiency reduction reaching almost a 2% relative difference. The absolute magnitude of volumetric efficiency penalty is low.

Diesel fuel may be trapped in and gas may permeate into a porous coating, resulting in deterioration of engine performance and emissions. A potential solution is to seal the combustion surface by encapsulating a porous the thermal barrier coating. An extra 5 μm layer of Silica $(96\%)^{69}$ was added on top of the best coating of each material family shown in Table 4 The objective of this investigation was to evaluate the system-level engine thermodynamic effect of a thermal barrier coating system that includes a sealing layer. Figure 19 shows a comparison of the drive-cycle-mean turbine outlet temperature and the BSFC reduction for cases with (squares) and without (circles) the sealing layer. The cases with the sealing layer showed slightly increased
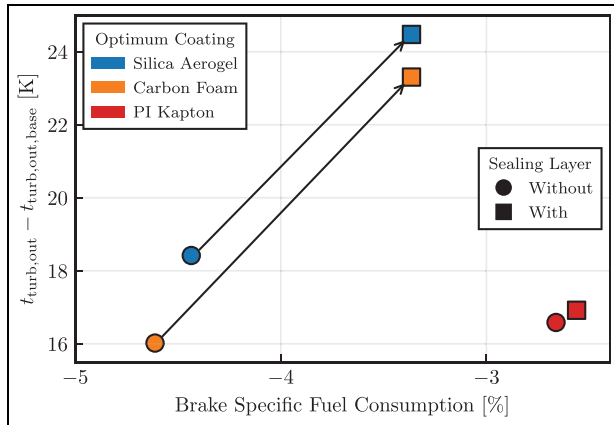
Figure 19. Comparison of the drive-cycle-mean turbine outlet temperature difference with the relative BSFC between coated and baseline. The coated cases were evaluated without (circles) and with (squares) a sealing layer.

exhaust temperatures and a penalty in fuel savings as compared to the cases without the sealing layer.

Conclusions

A constrained hierarchical optimization was performed to minimize heat transfer of a medium-duty diesel engine using multilayer-coated pistons subject to a structural integrity constraint. The output revealed the optimal materials and their corresponding thickness for a real-world drive cycle. Over 800 materials were investigated, and the optimization required more than one million evaluations of the non-road transient drive cycle. Only real materials were tested to ensure a realizable result and the existence of the thermal and mechanical properties. The material properties were acquired either from the literature or from commercial software packages. This study elucidates the importance of including mechanical considerations in the design of thermal barrier coatings.

A calibrate system-level model was used to provide boundary conditions to the uncoupled optimization. The uncoupled in-cylinder heat transfer reduction, Γ_{net}, closely followed the coupled value in an a posteriori comparison. The analytical solution methodology substantially increased the computational efficiency, allowing a wide array of materials to be tested over a full drive cycle calculation. Durability considerations were found to be important for coating design. The highest energy release rates were found in the mid-coating area during the cycle with the highest instantaneous surface temperature of the transient drive cycle. At this time, the surface was cooling while the rest of the interior wall was still undergoing heating. A trade-off between the in-cylinder heat transfer reduction and the coating structural integrity was quantified.

In this study, the maximum piston-coating interface temperature was significantly below the service limit and did not penalize the optimal coating thickness. The mechanically unconstrained scenario gave rise to the trivial solution, that is, the best thermal insulation was achieved with the thickest possible coating. However, the mechanical toughness constraint impacted a significant number of material candidates. Ceramics and glasses with outstanding thermal properties were penalized for having maximum energy release rate higher than their limit. The polymers had intermediate engine thermal insulation performance with small penalties due to the mechanical constraint. The metals had the poorest thermal insulation properties with the best mechanical properties. A trade-off between the net and pumped heat transfer was realized from the optimization results. Reduced levels of net heat transfer were accompanied by higher pumped heat transfer. The volumetric efficiency penalty was only up to 2% over the drive cycle.

The 10 highest-performing coating materials identified via uncoupled optimization were tested using a fully coupled system-level simulation. The uncoupled and coupled net heat transfer reduction showed good agreement. The optimal coatings gave significant heat transfer reduction, which led to fuel savings. The fuel consumption reduction accounted for only a fraction of the reduced heat loss. The exhaust enthalpy, for the example of the Carbon Foam, was found to increase by almost 6% in spite of 4% less fuel being used during the drive cycle.

Finally, the thermodynamic effect of an extra sealing layer to prevent air/fuel migration in a porous coating was investigated. A sealing layer on a thermal barrier coating system may increase exhaust temperature while penalizing the BSFC gains that would have been obtained from the main insulation layer alone.

member of the OSG Consortium, which is supported by the National Science Foundation and the U.S. Department of Energy's Office of Science.

ORCID iD

Georgios Koutsakis   https://orcid.org/0000-0002-8108-2591

References

1. Myers PS. Ceramics for transportation engines—siren or solution. *Appl Mech Rev* 1989; 42: 53–69.
2. Uchida N. A review of thermal barrier coatings for improvement in thermal efficiency of both gasoline and diesel reciprocating engines. *Int J Engine Res* 2022; 23: 3–19.
3. Kosaka H, Wakisaka Y, Nomura Y, et al. Concept of "temperature swing heat insulation" in combustion chamber walls, and appropriate thermo-physical properties for heat insulation coat. *SAE Int J Engines* 2013; 6(1): 142–149.
4. Serrano JR, Arnau FJ, Martin J, et al. Analysis of engine walls thermal insulation: performance and emissions. SAE technical paper 2015-01-1660, 2015. DOI: 10.4271/2015-01-1660.
5. Kawaguchi A, Iguma H, Yamashita H, et al. Thermo-swing wall insulation technology – a novel heat loss reduction approach on engine combustion chamber. SAE technical paper 2016-01-2333, 2016. DOI: 10.4271/2016-01-2333.
6. Andruskiewicz P, Najt P, Durrett R, Biesboer S, Schaedler T and Payri R. Analysis of the effects of wall temperature swing on reciprocating internal combustion engine processes. *Int J Engine Res* 2018; 19: 461–473.
7. Killingsworth N, Powell T, O'Donnell R, et al. Modeling the effect of thermal barrier coatings on HCCI engine combustion using CFD Simulations with conjugate heat transfer. SAE technical paper 2019-01-0956, 2019. DOI: 10.4271/2019-01-0956.
8. Caputo S, Millo F, Cifali G and Pesce FC. Numerical investigation on the effects of different thermal insulation strategies for a passenger car diesel engine. *SAE Int J Engines* 2017; 10: 2154–2165.
9. Powell T, O'Donnell R, Hoffman M, et al. Experimental investigation of the relationship between thermal barrier coating structured porosity and homogeneous charge compression ignition engine combustion. *Int J Engine Res* 2021; 22: 88–108.
10. Yamashita C, Yamashita H, Kawaguchi A, et al. Development of the heat insulation coating by temperature swing for the combustion chamber wall of gasoline engine (in japanese). In: *2019 JSAE annual congress*, Yokohama, Japan, 22–24 May 2019.
11. Olmeda P, Martín J, Novella R and Blanco-Cavero D. Assessing the optimum combustion under constrained conditions. *Int J Engine Res* 2020; 21(5): 811–823.
12. Chérel J, Zaccardi JM, Bouteiller B and Allimant A. Experimental assessment of new insulation coatings for lean burn spark-ignited engines. *Oil Gas Sci Technol* 2020; 75: 11.
13. Mohr D, Shipp T and Lu X. The thermodynamic design, analysis and test of cummins' supertruck 2 50% brake thermal efficiency engine system. SAE technical paper, 2019-01-0247, 2019. DOI:10.4271/2019-01-0247.
14. Watanabe K, Uchida N, Yokogawa K, et al. What are the barriers against brake thermal efficiency beyond 55% for HD diesel engines? SAE technical paper, 2021-24-0039, 2021. DOI: 10.4271/2021-24-0039.
15. O'Connor J, Borz M, Ruth D, et al. Optimization of an advanced combustion strategy towards 55% BTE for the Volvo SuperTruck Program. *SAE Int J Engines* 2017; 10(3): 1217–1227.
16. Assanis DN, Wiese K, Schwarz E, et al. The effects of ceramic coatings on diesel engine performance and exhaust emissions. SAE technical paper 910460, 1991. DOI: 10.4271/910460.
17. Osawa K, Kamo R and Valdmanis E. Performance of thin thermal barrier coating on small aluminum block diesel engine. SAE technical paper 910461, 1991. DOI: 10.4271/910461.
18. Chan SH and Khor KA. The effect of thermal barrier coated piston crown on engine characteristics. *J Mater Eng Perform* 2000; 9(1): 103–109.
19. Mendera KZ. Effectiveness of plasma sprayed coatings for engine combustion chamber. *SAE Trans* 2000; 109: 3112–3121.
20. Schihl P, Schwarz E and Bryzik W. Performance characteristics of a low heat rejection direct-injection military diesel engine retrofitted with thermal barrier coated pistons. *J Eng Gas Turbine Power* 2001; 123(3): 644–651.
21. Kamo R, Mavinahally NS, Kamo L, et al. Injection characteristics that improve performance of ceramic coated diesel engines. SAE technical paper 890292, SAE International, 1999. DOI: 10.4271/1999-01-0972.
22. Dickey DW. The effect of insulated combustion chamber surfaces on direct-injected diesel engine performance, emissions and combustion. SAE technical paper 890292, 1989. DOI: 10.4271/890292.
23. Cheng WK, Wong VW and Gao F. Heat transfer measurement comparisons in insulated and non-insulated diesel engines. SAE technical paper 890570, 1989. DOI: 10.4271/890570.
24. Andrie M, Kokjohn S, Paliwal S, et al. Low heat capacitance thermal barrier coatings for internal combustion engines. SAE technical paper 2019-01-0228, 2019, pp.1–13. DOI: 10.4271/2019-01-0228.
25. Kawaguchi A, Wakisaka Y, Nishikawa N, et al. Thermo-swing insulation to reduce heat loss from the combustion chamber wall of a diesel engine. *Int J Engine Res* 2019; 20: 805–816.

26. Hoffman MA, Lawler BJ, Güralp OA, Najt PM and Filipi ZS. The impact of a magnesium zirconate thermal barrier coating on homogeneous charge compression ignition operational variability and the formation of combustion chamber deposits. *Int J Engine Res* 2015; 16(8): 968–981.

27. Filipi Z, Hoffman M, O'Donnell R, Powell T, Jordan E and Kumar R. Enhancing the efficiency benefit of thermal barrier coatings for homogeneous charge compression ignition engines through application of a low-k oxide. *Int J Engine Res* 2021; 22: 1906–1923.

28. Keskinen K, Vera-Tudela W, Wright YM and Boulouchos K. Experimental investigation of wall heat transfer due to spray combustion in a high-pressure/high-temperature vessel. *Int J Engine Res* 2021; 22: 3489–3502.

29. Powell T. Impacts of thermal barrier coating morphology and catalytic properties on low temperature combustion engine in-cylinder processes. PhD Thesis, Clemson University, Clemson, SC, 2018.

30. Somhorst J, Oevermann M, Bovo M and Denbratt I. Evaluation of thermal barrier coatings and surface roughness in a single-cylinder light-duty diesel engine. *Int J Engine Res* 2021; 22: 890–910.

31. Gingrich E, Tess M, Korivi V, et al. The impact of piston thermal barrier coating roughness on high-load diesel operation. *Int J Engine Res* 2021; 22: 1239–1254.

32. Gatowski JA. Evaluation of a selectively-cooled single-cylinder 0.5-L diesel engine. *SAE Trans* 1990; 99: 1580–1591.

33. Woschni G, Spindler W and Kolesa K. Heat insulation of combustion chamber walls — A measure to decrease the fuel consumption of I.C. engines? *SAE Trans* 1987; 96: 269–279.

34. Furuhama S and Enomoto Y. Heat transfer into ceramic combustion wall of internal combustion engines. *SAE Trans* 1987; 95: 17–30.

35. Osada H, Watanabe H, Onozawa Y, et al. Experimental analysis of heat-loss with different piston wall surface conditions in a heavy-duty diesel engine. In: *The Proceedings of the International symposium on diagnostics and modeling of combustion in internal combustion engines*, Okayama, Japan, 25–28 July 2017, p.B204. The Japan Society of Mechanical Engineers. DOI: 10.1299/jmsesdm.2017.9.B204.

36. Alkidas AC. Performance and emissions achievements with an uncooled heavy-duty, single-cylinder diesel engine. SAE technical paper 890144, 1989. SAE International. DOI: 10.4271/890144.

37. Huang JC and Borman GL. Measurements of instantaneous heat flux to metal and ceramic surfaces in a diesel engine. *SAE Trans* 1987; 96: 66–81.

38. Hendricks TL, Splitter DA and Ghandhi JB. Experimental investigation of piston heat transfer under conventional diesel and reactivity-controlled compression ignition combustion regimes. *Int J Engine Res* 2014; 15(6): 684–705.

39. Kokjohn SL, Hanson RM, Splitter DA and Reitz RD. Fuel reactivity controlled compression ignition (RCCI): a pathway to controlled high-efficiency clean combustion. *Int J Engine Res* 2011; 12(3): 209–226.

40. Kokjohn S, Hanson R, Splitter D, Kaddatz J and Reitz RD. Fuel reactivity controlled compression ignition (RCCI) combustion in light- and heavy-duty engines. *SAE Int J Engines* 2011; 4(1): 360–374.

41. Koutsakis G, Miles S and Ghandhi J. Assessment of in-cylinder thermal barrier coatings over a full vehicle drive cycle. SAE technical paper 2021-01-0456, 2021. SAE International. DOI: 10.4271/2021-01-0456.

42. Koutsakis G and Ghandhi J. Analytical solution of unsteady heat conduction in multilayer internal combustion engine walls. *Appl Therm Eng* 2022; 118681. DOI: 10.1016/j.applthermaleng.2022.118681

43. Babu A, Koutsakis G, Kokjohn S, et al. Experimental and analytical study of temperature swing piston coatings in a medium-duty diesel engine. SAE technical paper 2022-01-0442, 2022. DOI:10.4271/2022-01-0442

44. Beardsley MB. *Potential use of quasicrystalline materials as thermal barrier coatings for diesel engine components*. Ames, IA: Iowa State University, 2008.

45. Yonushonis TM. *Thick thermal barrier coatings for diesel components*. Cleveland, OH: NASA Lewis Research Center, 1991.

46. Saad D, Saad P, Kamo L, et al. Thermal barrier coatings for high output turbocharged diesel engine. SAE technical paper, 2007-01-1442, 2007. DOI: 10.4271/2007-01-1442.

47. Tricoire A, Kjellman B, Wigren J, Vanvolsem M and Aixala L. Insulated piston heads for diesel engines. *J Therm Spray Technol* 2009; 18(2): 217–222.

48. Uchida N and Osada H. A new piston insulation concept for heavy-duty diesel engines to reduce heat loss from the wall. *SAE Int J Engines* 2017; 10(5): 2565–2574.

49. Schaedler T, Andruskiewicz P, Durrett R, et al. Temperature-following thermal barrier coatings for high efficiency engines. In: *DOE vehicle technologies annual merit review*, Arlington, VA, 18–21 June 2018. U.S. Department of Energy.

50. Thibblin A and Olofsson U. A study of suspension plasma-sprayed insulated pistons evaluated in a heavy-duty diesel engine. *Int J Engine Res* 2020; 21(6): 987–997.

51. Koutsakis G, Begley MR, Hutchinson JW, et al. Fracture-based transient thermo-mechanical analysis of reciprocating engine thermal barrier coatings. *J Eng Fract Mech* 2022; 108568. DOI: 10.1016/j.engfracmech.2022.108568.

52. Koutsakis G. Unsteady heat conduction and fracture mechanics in multilayer engine coatings. PhD Thesis, University of Wisconsin-Madison, 2022.

53. Koutsakis G, Saputo J, Gingrich E, et al. Delamination failure on high-output diesel engine thermal barrier coatings. SAE technical paper 2022-01-0440, 2022. SAE International. DOI: 10.4271/2022-01-0440

54. Wurzenberger JC, Wanker R and Schüßler M. Simulation of exhaust gas aftertreatment systems-thermal behavior during different operating conditions. SAE technical paper 2008-01-0865, 2008. DOI: 10.4271/2008-01-0865.

55. Papetti V, Eggenschwiler PD, Della Torre A, et al. Heat transfer analysis of catalytic converters during cold starts. SAE technical paper 2019-24-0163, 2019.

56. Papetti V, Dimopoulos Eggenschwiler P, Della Torre A, et al. Instationary heat and mass transfer phenomena in additive manufactured open cell polyhedral structures for automotive catalysis. *Chem Eng Sci* 2021; 234: 116448.

57. Arnau FJ, Martín J, Piqueras P and Auñón. Effect of the exhaust thermal insulation on the engine efficiency and the exhaust temperature under transient conditions. *Int J Engine Res* 2021; 22(9): 2869–2883.

58. DieselNetcom. Non-road transient cycle standard, https://dieselnet.com/standards/cycles/nrtc.php (2020).

59. Heywood JB. *Internal combustion engine fundamentals*. New York, NY: McGraw-Hill, 1988.

60. Koutsakis G, Nellis GF and Ghandhi JB. Surface temperature of a multi-layer thermal barrier coated wall subject to an unsteady heat flux. *Int J Heat Mass Transf* 2020; 155: 120187. DOI: 10.1016/j.ijheatmasstransfer. 2020.119645

61. Koutsakis G and Ghandhi JB. An analytical approach for calculating instantaneous multilayer-coated wall surface temperature in an engine. *SAE Int J Adv Curr Pract Mobil* 2020; 2: 1303–1313. DOI: 10.4271/2020-01-0160

62. Tsutsumi Y, Nomura K and Nakamura N. Effect of mirror-finished combustion chamber on heat loss. SAE technical paper 902141, 1990; DOI: 10.4271/902141.

63. Saputo JC, Smith GM, Lee H, Sampath S, Gingrich E and Tess M. Thermal swing evaluation of thermal barrier coatings for diesel engines. *J Therm Spray Technol* 2021; 29: 1943–1957.

64. Rabiner LR and Gold B. *Theory and application of digital signal processing*. Englewood Cliffs, NJ: Prentice-Hall, 1975. pp.63–65.

65. Morel T, Keribar R and Blumberg PN. Cyclical thermal phenomena in engine combustion chamber surfaces. SAE technical paper 1985. DOI: 10.4271/850360.

66. Gamma Technologies. *GT-SUITE*. Westmont, IL: Gamma Technologies, 2020.

67. Virtanen P, Gommers R, Oliphant TE, et al. Author Correction: SciPy 1.0: Fundamental Algorithms for Scientific Computing in Python. *Nat Methods* 2020; 17: 352–272.

68. Thain D, Tannenbaum T and Livny M. Distributed computing in practice: the condor experience. *Concurr Comput* 2005; 17(2-4): 323–356.

69. ANSYS. *Granta Selector*. ANSYS, Inc, 2020. https:// www.ansys.com/products/materials/granta-selector

70. Squire TH, Milos FS and Hartlieb GC. Aerospace materials property database (TPSX). *J Spacecr Rockets* 2009; 46(3): 733–736.
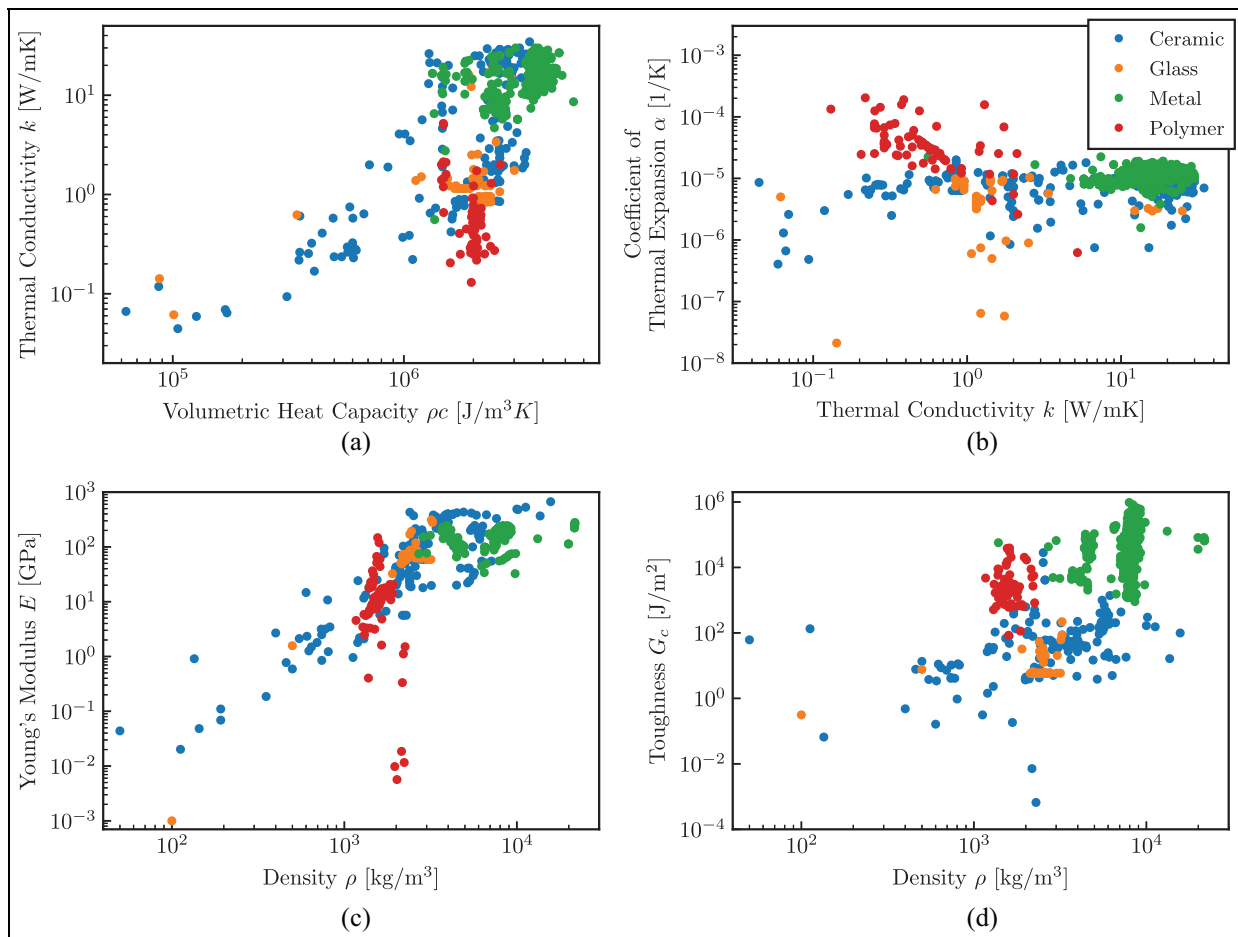
Appendix

Figure A1. In-house thermomechanical property library of material candidates (ceramics, glasses, metals, and polymers) used in the optimization study. Various properties are compared including (a) thermal conductivity k and volumetric heat capacity ρc, (b) coefficient of thermal expansion α and thermal conductivity k, (c) Young's modulus E and density ρ, and (d) toughness G_c and density ρ.